The University of Maine
DigitalCommons@UMaine

Marine Sciences Faculty Scholarship | School of Marine Sciences

9-20-2012

Improved irradiances for use in ocean heating, primary production, and photo-oxidation calculations

Curtis D. Mobley
Sequoia Scientific, Inc.

Emmanuel S. Boss
University of Maine, emmanuel.boss@maine.edu

Follow this and additional works at: https://digitalcommons.library.umaine.edu/sms_facpub

Part of the Oceanography and Atmospheric Sciences and Meteorology Commons

Repository Citation

Mobley, Curtis D. and Boss, Emmanuel S., "Improved irradiances for use in ocean heating, primary production, and photo-oxidation calculations" (2012). *Marine Sciences Faculty Scholarship*. 160.
https://digitalcommons.library.umaine.edu/sms_facpub/160

This Article is brought to you for free and open access by DigitalCommons@UMaine. It has been accepted for inclusion in Marine Sciences Faculty Scholarship by an authorized administrator of DigitalCommons@UMaine. For more information, please contact um.library.technical.services@maine.edu.

Improved irradiances for use in ocean heating, primary production, and photo-oxidation calculations

Curtis D. Mobley[1,*] and Emmanuel S. Boss[2]

[1]Sequoia Scientific, Inc., 2700 Richards Road, Suite 107, Bellevue, Washington 98005, USA

[2]School of Marine Sciences, 5706 Aubert Hall, University of Maine, Orono, Maine 04469, USA

*Corresponding author: curtis.mobley@sequoiasci.com

Received 25 May 2012; revised 30 July 2012; accepted 14 August 2012;
posted 16 August 2012 (Doc. ID 169414); published 14 September 2012

Accurate calculation of underwater light is fundamental to predictions of upper-ocean heating, primary production, and photo-oxidation. However, most ocean models simulating these processes do not yet incorporate radiative transfer modules for their light calculations. Such models are often driven by above-surface, broadband, daily averaged irradiance or photosynthetically available radiation (PAR) values obtained from climatology or satellite observations, sometimes without correction for sea-surface reflectance, even though surface reflectance can reduce in-water values by more than 20%. We present factors computed by a radiative transfer code that can be used to convert above-surface values in either energy or quantum units to in-water net irradiance, as needed for calculations of water heating, and to in-water PAR, as needed for calculations of photosynthesis and photo-oxidation. © 2012 Optical Society of America

OCIS codes: 010.4450, 010.5620.

1. Introduction

Numerous studies have shown that oceanic phytoplankton affect upper-ocean thermal structure via absorption of solar irradiance at visible wavelengths; the review paper by Dickey and Falkowski [1] summarizes two dozen papers on this subject. Most of these studies used one-dimensional (depth dependence only) models in which visible-wavelength irradiance was distributed with depth as an input to heating-rate calculations for the mixed layer. The models have varying degrees of sophistication. The simplest models for in-water irradiance (e.g., [2,3]) use one or more exponentials to parameterize the depth decay of broadband irradiance in terms of an assumed Jerlov water type or e-folding depth. The more sophisticated models of Ohlmann *et al.* [4–6] use parameterizations of solar irradiance transmission through the air–water interface and water column as functions of the solar zenith angle, cloud cover, wind speed, wavelength, and chlorophyll concentration. Those irradiance parameterizations were obtained by analytical fits to more exact numerical calculations using the computationally intensive HydroLight radiative transfer code [7–9].

Similar studies have been done using large-scale, three-dimensional (3D) general circulation models (GCMs), often forced with climatological or satellite-derived inputs for above-surface, broadband irradiance and prescribed in-water attenuation rates. Schneider and Zhu [10] used a coupled atmosphere–ocean GCM to study the effects of two different models of light penetration on upper-ocean heating and circulation. The first model assumed that all solar irradiance was absorbed in the uppermost layer of the ocean model, and the second model used a depth-dependent irradiance with a fixed attenuation rate of $K_d = -(d \ln E_d/dz) = 0.067\ \mathrm{m}^{-1}$ [a 15 m e-folding depth; z is depth and E_d is defined in Eq. (2) below], which allowed solar irradiance to penetrate deeper within the water. Nakamoto *et al.* [11,12] and

1559-128X/12/276549-12$15.00/0
© 2012 Optical Society of America

Murtugudde *et al.* [13] then studied biomass effects on heating in ocean GCMs for an irradiance profile with a constant K_d value versus one in which K_d depended on time- and space-dependent chlorophyll concentrations. Similar studies by Rochford *et al.* [14] and Kara *et al.* [15] obtained both E_d and K_d from SeaWiFS data and compared the results with those obtained using constant K_d values. Sweeney *et al.* [16] compared single- and double-exponential functions for depth dependence of near-ultraviolet and visible irradiance in their effect on ocean heating and circulation. They assumed the solar zenith angle to be 0° in a clear sky; the in-water chlorophyll concentration was taken from SeaWiFS data.

The above-cited models parameterized light penetration in terms of K_d values that were external, forcing functions imposed on the ocean GCM. The models thus considered biological influences on upper-ocean heating and circulation, but there was no feedback to biology. Only recently have global-scale ocean GCMs begun to include biogeochemical modules that predict chlorophyll and related biological quantities as state variables [17–19]. Likewise, only a few studies have looked at atmospheric effects related to biologically influenced sea-surface temperatures (SSTs). Shell *et al.* [20] first ran an ocean GCM for in-water attenuation determined either by Paulson and Simpson [2] or by SeaWiFS chlorophyll values to compute the corresponding SSTs. They then used those SSTs as inputs to an atmospheric GCM. Wetzel *et al.* [21] ran a fully coupled atmosphere–ocean GCM including a nitrogen, phytoplankton, zooplankton, and detritus biological module. They compared a "fixed" ocean, which assumed a constant PAR e-folding depth of 11 m, with a "green" ocean, which obtained K_d from the evolving chlorophyll value. Both Shell *et al.* [20] and Wetzel *et al.* [21] found that the biological effects on in-water light attenuation led to significant differences not just in the upper ocean, but also in the atmosphere over both water and land via the coupling between SST and atmospheric inputs of heat and moisture. Consequently, the most recent and sophisticated global-scale models [19,22] have included fully coupled hydrodynamical–biological components and chlorophyll-dependent in-water light propagation based on [6]. The Ocean Atmosphere Spectral Irradiance Model (OASIM) [23] provides spectral irradiances either above or just below the sea surface (at 25 nm resolution in the PAR wavelengths 400–700 nm, with 33 bands in total covering 0.2–4.0 μm). OASIM is based on the RADTRAN clear-sky atmospheric irradiance model [24] with various modifications such as the inclusion of clouds and an expanded wavelength range. Irradiance transmission through the sea surface is computed by simple analytical parameterizations. OASIM has been used in coupled ocean ecosystem models [25] with a simple optical model to propagate irradiances to depth, and it is a part of the NASA Ocean Biogeochemical Model [26].

These studies differed in their GCMs, study areas, sources for chlorophyll (satellite, climatology, or predicted), and overall sophistication. Nevertheless, they all reached the same general conclusion: it is imperative that in-water light propagation be accurately computed. Phytoplankton absorption of visible light affects upper-ocean heating and consequently upper-ocean mixing and currents, SST, and finally atmospheric heating and circulation, all of which have feedbacks to the biology.

The proper way to incorporate light into GCMs is via fully coupled hydrodynamic–biological–optical ecosystem models in which the optical module is a radiative transfer code that computes the spectral irradiance using the current values for chlorophyll and other water-column constituents, incident sky radiance, and wind speed (i.e., ocean wave state). The HydroLight code computes in-water irradiances to roughly 1% accuracy for any water or atmospheric conditions, but it requires far too much computational time to be practicable for use in ecosystem models requiring light calculations at many grid point and time steps. However, the recently developed EcoLight-S(ubroutine) [27] radiative transfer numerical model is sufficiently fast to be computationally practicable for incorporation into three-dimensional (3D) ocean ecosystem models. The EcoLight-S code is designed to replace simple and often inaccurate analytical models for in-water irradiance with more accurate calculations. EcoLight-S solves the radiative transfer equation (RTE) given the depth profiles of water constituents (typically parameterized as concentrations of chlorophyll, dissolved matter, and minerals, which are then converted to absorption and scattering values via bio-optical models) and external forcing (incident radiance onto the sea surface, wind speed) to obtain the spectral radiance as a function of depth, direction, and wavelength. Irradiances are then obtained from the computed radiance. One call to EcoLight-S can compute spectral irradiance from 300–1000 nm throughout the euphotic zone in a fraction of a second of computing time. The errors in the associated PAR profiles are less than 10%, compared to values computed by HydroLight with more than 1000 times the computational cost. The computed irradiance is then used in computations of primary production and water heating [28]. When judiciously employed using its various optimizations, EcoLight-S can replace analytical irradiance models with only a few tens of percent increase in total ecosystem simulation run times [29]. However, the use and evaluation of EcoLight-S within 3D coupled hydrodynamic–biological ecosystem models is still in its infancy for regional-scale ecosystem simulations [30]. Incorporation of in-water RTE-solving radiative transfer modules into global-scale models, although now computationally practicable, is still some years in the future.

The GCMs currently used for global-scale climate studies have a number of common features. Although

they may use shorter time steps for computational stability, they typically use daily (24 h) averaged irradiance values that are updated at most once a day (often with values interpolated from monthly averages). The models typically have spatial resolutions of the order or 1° in latitude and longitude, and upper-ocean depth resolutions of the order of 10 m. Their hydrodynamic calculations are very sophisticated. However, the biological modules of these models are at best simple (e.g., driven by daily averaged PAR rather than by instantaneous spectral irradiance) and may not even include biomass as a predicted state variable. In models without a biological module, the biological effects on upper-ocean heating are usually incorporated by parameterizing biomass in terms of the chlorophyll concentration, which is taken from climatology or satellite-derived estimates. Upper-ocean heating is then computed using very simple models for the propagation of solar irradiance with depth. Studies may be carried out for decades or even centuries of simulated time. The need for computational efficiency in global-scale, long-term simulations places a severe constraint on the formulation of the models.

Few of the 3D studies cited above mention how above-surface irradiance, $E_d(\text{air})$, is transmitted through the sea surface to initialize the in-water model for $E_d(z)$. The exceptions are Sweeney *et al.* [16], who reduced the above-surface irradiance by 6% to obtain values just below the sea surface; studies (e.g., [22]) employing the Community Climate System Model version 3 [19], which uses the parameterization of [6]; and the NASA Ocean Biogeochemistry Model, which uses OASIM to initialize the input spectral irradiances. This leaves us to speculate that many GCMs are using above-surface values for in-water values at depths of $z = 0$ just below the sea surface. No ocean GCM appears to incorporate a latitude-, time-, and wind-dependent factor to transmit above-surface irradiance through the sea surface. However, as shown below, the surface transmittance of above-surface, daily averaged E_d varies from a high of 96% to less than 80%, depending on the latitude and time of year (i.e., depending on the cumulative effects of the varying Sun zenith angle during the day), sky conditions and sea state. The use of above-surface E_d to initialize in-water values thus can result in systematic overestimation of in-water irradiance by as much as 20% regardless of what model is used to propagate E_d to depth. Such errors may have significant effects on upper-ocean heating and on primary production in models with a biological module. Most ocean GCMs use 400–700 nm for their PAR calculations, so we consider that range for the calculations below. However, it must be noted that wavelengths outside this range also contribute to water heating and photo-oxidation, which is yet another argument for replacing currently used analytical models of short-wave light penetration with codes such as EcoLight-S.

In addition to the GCMs reviewed above, other types of models also need accurate light values. Models for primary production, photo-oxidation, and fluorescence (e.g., [31–34]) require PAR in quantum units (defined below). Although the model of Behrenfeld *et al.* [31] partially corrects for surface effects and differences in plane and scalar irradiances, none of the cited models fully accounts for surface effects including solar zenith angle and wind speed.

We are thus in the situation where numerous studies have shown the importance of accurate in-water light calculations, but where imbedded radiative transfer codes have yet to be employed. Ideally, ecosystem simulations would be performed with coupled ocean–atmosphere models including full radiative transfer calculations of the light field, which could automatically account for the effects of sky conditions, surface waves, and other environmental parameters. Such simulations are just now becoming possible (e.g., with fast codes such as EcoLight-S for the in-water calculations), but they are still severely limited by the computational constraints of long-term, global-scale simulations. Given the increasing importance of GCMs and other types of models in simulations of the global ecosystem and climate change and the need for both accuracy and computational efficiency, this paper therefore presents surface transmission factors that can be used to convert above-surface, daily averaged irradiance and PAR values into below-surface values, either in energy or quantum units, without significant computational expense. We hope that these factors can improve simulations for the near term, pending the development of more sophisticated models incorporating radiative transfer modules.

Section 2 defines terms and describes the radiative transfer numerical simulations used to generate the needed surface transmission factors. Section 3 then discusses factors that convert above-surface irradiances to various below-surface values, as may be useful for different types of simulations. Section 4 summarizes and shows where to download the data files.

2. Radiative Transfer Simulations

Let $L(z, \theta, \phi, \lambda)$ be the spectral radiance [$\mathrm{W\,m^{-2}\,sr^{-1}\,nm^{-1}}$] as a function of depth z, polar angle θ, azimuthal angle ϕ, and wavelength λ. Then the downwelling spectral plane irradiance is given by

$$E_d(z, \lambda) = \int_0^{2\pi} \int_0^{\pi/2} L(z, \theta, \phi, \lambda) \cos\theta \sin\theta \mathrm{d}\theta \mathrm{d}\phi. \quad (1)$$

Here z is measured positive downward from the mean sea surface at $z = 0$, and $\theta = 0$ in the $+z$ or nadir direction. Depth 0 denotes in-water values just below the mean sea surface; a depth argument of "air" will refer to values just above the surface. A corresponding integration over the upward directions defines $E_u(z, \lambda)$. With the exception of the NASA Ocean Biogeochemical Model, the GCMs cited above all use irradiances integrated over the visible wavelengths where light best penetrates the ocean,

typically 400–700 nm. We use E without a wavelength argument to denote band-integrated irradiances, e.g.,

$$E_d(z) = \int_{400}^{700} E_d(z,\lambda)\mathrm{d}\lambda, \tag{2}$$

which has energy units of $\mathrm{W\,m^{-2}}$. The band-integrated, net downward irradiance, $E_{\mathrm{net}} = E_d - E_u$, is the measure of light used to compute the time rate of change of temperature T via

$$\frac{dT}{dt} = \frac{1}{\rho c_p}\frac{dE_{\mathrm{net}}}{dz}, \tag{3}$$

where ρ is the density and c_p is the specific heat of sea water. E_u is usually only a few percent of E_d, so E_{net} in Eq. (3) is often approximated by E_d.

It is the number of photons absorbed, not their individual energies or directions of propagation, that governs photosynthesis and photo-oxydation. Thus the spectral scalar irradiance

$$E_o(z,\lambda) = \int_0^{2\pi}\int_0^{\pi} L(z,\theta,\phi,\lambda)\sin\theta\mathrm{d}\theta\mathrm{d}\phi \tag{4}$$

is the radiometric quantity used to compute photosynthetically available radiation (PAR) for use in computations of photosynthesis. PAR has quantum units of photons $\mathrm{m^{-2}\,s^{-1}}$, not energy units of $\mathrm{W\,m^{-2}}$, and it is obtained from $E_o(z,\lambda)$ via

$$\mathrm{PAR}_o = \int_{400}^{700} E_o(\lambda)\frac{\lambda}{hc}\mathrm{d}\lambda. \tag{5}$$

(Some papers use the 350–700 nm wavelength range to compute PAR.) The factor λ/hc, where h is Planck's constant and c is the speed of light, in the integration over wavelength converts energy units to quantum units.

The studies referenced in the introduction use a variety of terminology and are sometimes vague in defining exactly what measure of light is used in their calculations. Some papers refer only to "solar flux" or "visible radiation" without specifying the wavelength range or other details. Others confusingly use "PAR" as a synonym for irradiance in energy units in the 400–700 nm band. We will be more precise. We use E for quantities in energy units and PAR for quantities in quantum units. For example, the NASA [35] and MERIS [36] PAR products are properly in quantum units, but they are above-surface quantities computed using $E_d(\lambda)$ in Eq. (5). We denote this quantity by PAR_d to distinguish it from PAR_o as defined in Eq. (5) using $E_o(\lambda)$. Models with a biological module that computes photosynthesis using PAR, and that are forced by these PAR databases, thus need to convert $\mathrm{PAR}_d(\mathrm{air})$ values to $\mathrm{PAR}_o(0)$. Likewise, use of above-surface E_d values to initialize in-water-heating calculations requires conversion of $E_d(\mathrm{air})$ to $E_{\mathrm{net}}(0)$, with both in energy units.

The depth profiles of $E_{\mathrm{net}}(z)$ and $\mathrm{PAR}_o(z)$ away from the sea surface are determined by the water absorbing and scattering properties. However, the values just below the surface are determined primarily by the Sun and sky radiance incident onto the sea surface and by the surface roughness because both $E_{\mathrm{net}}(0)$ and $\mathrm{PAR}_o(0)$ result primarily from radiance transmitted through the surface, with only a small contribution (typically a few percent) from upwelling in-water radiance. This is illustrated for two Sun angles in Fig. 1, which also shows the differences in PAR correctly computed from E_o versus approximated using E_d. At depth 0, the curves group closely by Sun zenith angle, whereas at great depth, the curves group by chlorophyll value. The two curves for $\mathrm{Chl} = 5.0\ \mathrm{mg\,m^{-3}}$ have essentially reached their chlorophyll-determined asymptotic values by 30 m depth; the curves for $\mathrm{Chl} = 0.5\ \mathrm{mg\,m^{-3}}$ are almost asymptotic by 100 m. This figure suggests that it is possible to compute factors that convert above-surface irradiances to values just below the surface with the result that the factors will depend on sky conditions and wind speed, but only weakly on the chlorophyll concentration. Ecosystem or other models can then use the values at depth 0 to initialize their internal optical models for $\mathrm{PAR}_o(z)$ and $E_{\mathrm{net}}(z)$. It should be noted in this figure that the use of PAR computed from E_d would cause underestimation of the light available for photosynthesis by several tens of percent.

All of these quantities are standard outputs of the EcoLight-S radiative transfer code [27,37]. It was therefore straightforward to run EcoLight-S over the course of a day for a given latitude, time of year, wind speed, sky conditions, water chlorophyll concentration, and other inputs to generate the desired daily averaged radiometric quantities. Although the EcoLight-S code was developed for use in coupled ecosystem models and runs extremely fast when optimized in various ways [27], it gives exactly the

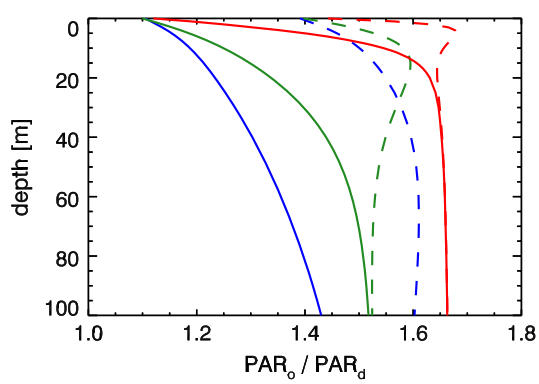

Fig. 1. (Color online) HydroLight-generated ratios of $\mathrm{PAR}_o(z)$ to $\mathrm{PAR}_d(z)$ for Sun zenith angles of 0° (solid curves) and 60° (dashed curves) in a clear sky. Each group of three near-surface curves is, left to right, Chl = 0.05 (blue), 0.5 (green), and 5.0 $\mathrm{mg\,m^{-3}}$ (red). The wind speed was 5 $\mathrm{m\,s^{-1}}$.

same irradiances as HydroLight when run in its unoptimized (and computationally slower) mode. The surface transmission factors shown below are therefore the same as would be computed by HydroLight with much more computational time and effort in generating the global- and annual-scale outputs shown below. The unoptimized EcoLight-S, rather than HydroLight, was used in the present calculations because it was convenient to set up a driver program that looped over the many inputs and then called EcoLight-S as a subroutine. (The standard HydroLight software is a stand-alone package that is designed for one RTE solution per run and is therefore less convenient for generation of the large output files needed for this study.) The polarization state of the incident sky radiance of course affects transmission by the sea surface. However, we did not have available a vector ocean–atmosphere code with which to compute transmission factors accounting for polarization. The effects of polarization on total radiance can be of the order of 10%, depending on direction and wavelength, when compared to unpolarized calculations, but those differences tend to average out when integrating over direction to compute irradiances.

EcoLight-S solves the scalar (unpolarized) azimuthally averaged RTE to obtain the spectral radiance as functions of depth, polar angle, and wavelength. Irradiances are then obtained from integration of the azimuthally averaged radiance over polar angle. The version of this code used here has a polar angle resolution of $\Delta\theta = 2°$. This results in the Sun being "smeared out" over a 2° wide θ band to obtain the corresponding azimuthally averaged solar radiance, even though the solar radiance itself is computed using the exact solar zenith angle. The runs used a wavelength resolution of 10 nm between 400–700 nm. This gives the same PAR values as 1 nm resolution to within 0.4%, but with one-tenth of the run time. The sea surface is statistically modeled via Cox-Munk [38,39] wind-speed wave-slope distributions for a given wind speed. Multiple scattering between tilted wave facets is included in the Monte Carlo computations of sea-surface reflectance and transmission functions. The mathematical details of these calculations are given in [8]. EcoLight-S called a modified RADTRAN sky irradiance model, which is based on the analytic model of Gregg and Carder [24], to compute the direct and diffuse spectral sky irradiances incident onto the sea surface. The modifications to RADTRAN consisted of extending its wavelength range from the original 400–700 nm to 300–1000 nm. An independent extension of RADTRAN is described in [40] with results that are extremely close (less that 0.05% difference in computed direct and diffuse irradiances) to those used here. RADTRAN clear-sky irradiances were modified by the model of Kasten and Czeplak [41] to account for clouds in the runs for an overcast sky. The RADTRAN code accounts for whitecaps via analytical models described in [24]. RADTRAN atmospheric inputs such as aerosol type, humidity, and pressure were taken to be typical open-ocean values; ozone values were take from climatology for the given latitude and day of year. The directional pattern of the radiance was computed using the semiempirical clear-sky model of Harrison and Coombes [42] as modified for clouds [43]. The magnitude of the normalized sky radiances so generated was scaled to reproduce the irradiances obtained from RADTRAN. The resulting spectral radiance from the Sun and sky was then used as input to the EcoLight-S. The same formulation of sky radiances is used in the standard HydroLight code.

The top panels of Fig. 2 show instantaneous values of $E_d(\text{air})$ and $E_{\text{net}}(0)$ as functions of solar zenith angle and wind speed for both clear and overcast sky conditions, as computed over both 400–700 nm [Fig. 2(a)] and 300–1000 nm [Fig. 2(b)] wavelength ranges. Figures 2(c) and 2(d) show the corresponding ratios $E_{\text{net}}(0)/E_d(\text{air})$. These are the multiplicative factors that would convert $E_d(\text{air})$ into $E_{\text{net}}(0)$. The lower left panel shows that $E_{\text{net}}(0)$ is anywhere from 0.785 to 0.965 times $E_d(\text{air})$ for a clear sky, depending on Sun angle and wind speed, for the 400–700 nm range. Factors for an overcast sky show little dependence on wind speed or Sun angle: the transmission remains between 0.93 and 0.95. For the 300–1000 nm range, the irradiances are roughly double the magnitudes of the values for 400–700 nm. However, the $E_{\text{net}}(0)/E_d(\text{air})$ factors usually differ by less than 1% for the two wavelength ranges. The largest difference is less than 3% and occurs for the Sun near the horizon and zero wind speed. Transmission factors such as $E_{\text{net}}(0)/E_d(\text{air})$ and the others discussed below are apparent optical properties (ratios of irradiances in this case) and are insensitive to radiance magnitudes.

Similar runs made for a clear sky using a marine aerosol (air mass type 1 in RADTRAN), 15 km horizontal visibility at the sea surface, the Sun at the zenith, and zero wind speed gave $E_d(\text{air}) = 467.78\ \text{W m}^{-2}$, $E_{\text{net}}(0) = 450.219\ \text{W m}^{-2}$, and a ratio of $E_{\text{net}}(0)/E_d(\text{air}) = 0.9625$. A simulation for a hazy sky with a continental aerosol (air mass type 10), and 5 km visibility gave $E_d(\text{air}) = 432.68\ \text{W m}^{-2}$, $E_{\text{net}}(0) = 411.638\ \text{W m}^{-2}$, and a ratio of $E_{\text{net}}(0)/E_d(\text{air}) = 0.9514$. This is a reduction of 7.5% in incident $E_d(\text{air})$ due to aerosol type and visibility, but only a 1% change in the transmission factor. The results are similar at other wind speeds and solar angles. The greatest difference in transmission factors occurs with the Sun is near the horizon and the sea surface is level, but even then the transmission factor changes by less than 5% between very clear and very hazy clear-sky conditions. Likewise, magnitude errors in $E_d(\text{air})$ when the Sun is very near the horizon resulting from the use of a plane–parallel atmospheric model rescale both above- and below-surface values and do not affect the ratios. Thus, differences in the transmission factors result from differences in the angular distribution of the incident solar and sky

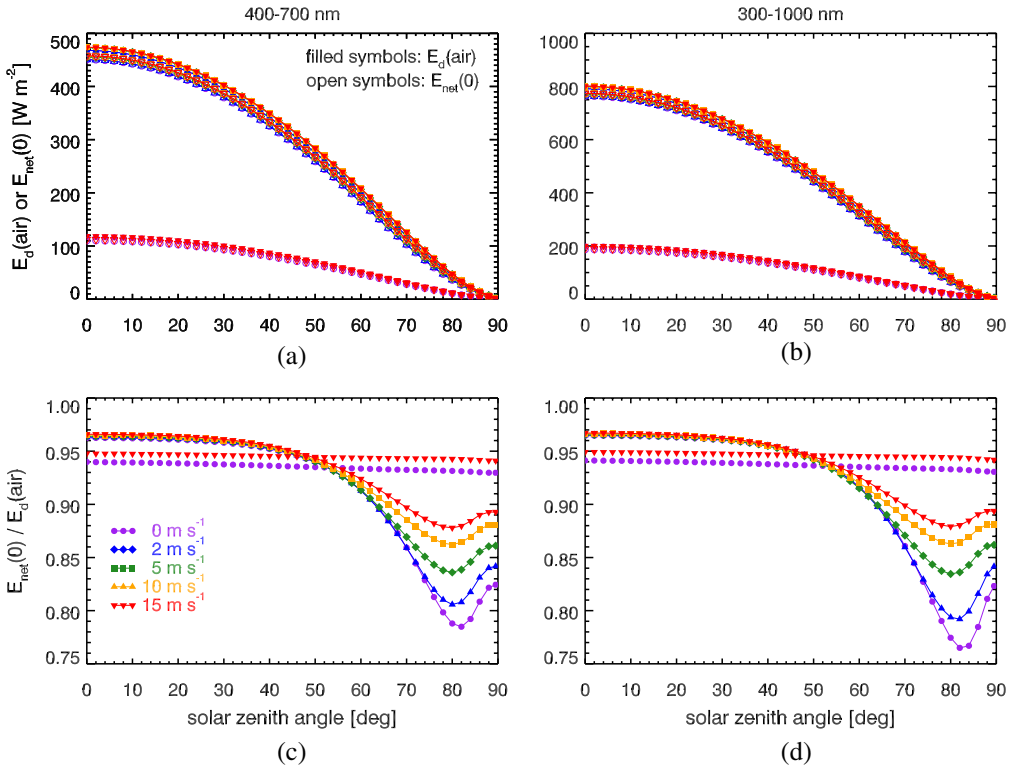

Fig. 2. (Color online) (a) E_d(air) and $E_{\mathrm{net}}(0)$ as a function of solar zenith angle and wind speed for both clear and overcast sky conditions, computed for the wavelength range of 400–700 nm. The wind speed is coded by symbol shape and color as shown in the bottom left panel. Curves with symbols connected by lines are for a clear sky; curves without lines connecting the symbols are for an overcast sky. (b) Corresponding curves for 300–1000 nm. (c) Multiplicative factor that converts E_d(air) into $E_{\mathrm{net}}(0)$ for the 400–700 nm range. (d) Corresponding values computed over the 300–1000 nm range. The chlorophyll concentration was 0.5 mg m^{-3}.

radiance, which are large for clear versus cloudy skies but not very dependent on the wavelength range or atmospheric conditions such as aerosol type. It also should be noted that transmission factors for daily averaged irradiances are very insensitive to wavelength range, aerosol type, and other such parameters because the instantaneous values for which the dependences on atmospheric conditions or wavelength are greatest occur for near-horizon solar angles where the irradiances are very small.

Simulations were therefore performed only for clear and overcast sky conditions, which do show much different transmission factors. Wind speeds of 0, 2, 5, 10, and 15 m s^{-1} and chlorophyll concentrations of 0.05, 0.5, and 5 mg m^{-3} were used. This range of chlorophyll concentrations spans values typically found from oligotrophic to bloom conditions. Test runs using chlorophyll values as high as 15 mg m^{-3} differed by less than a percent from chlorophyll = 5 values in the resulting transmission factors. This holds true even for PAR conversion factors, for which the chlorophyll-dependent upwelling radiance makes its greatest contribution. The chlorophyll values were converted to the absorption and scattering values needed to solve the RTE via a bio-optical model for Case 1 water [44]. Biological calculations are usually based on the 400–700 nm range, as is the NASA PAR product. We therefore used that wavelength range for subsequent calculations. As just seen, the same factors can be used with little error to rescale short-wavelength radiation (commonly taken to be 400–1000 nm) for water-heating calculations.

As the Sun goes from the zenith toward the horizon, the clear-sky curves in Figs. 2(c) and 2(d) reach minima near 80° zenith angle, but then they increase as the Sun approaches the horizon (90° zenith angle). This behavior warrants comment. The increase beyond 80°, which represents a higher fraction of incident irradiance getting into the ocean, results from a combination of surface Fresnel reflectance and diffuseness of the incident sky radiance. For a clear sky, the ratio of diffuse (background sky) irradiance to the total (sky plus direct solar) increases from about 25% (at 550 nm) when the Sun is at the zenith, to 40% at a solar zenith angle of 60°, 50% at 70°, 75% at 80°, and 99.8% at 88°. When the Sun is high in the sky, the Fresnel reflectance of the sea surface is low (less than 10% for incident angles less than 65°) and most of the radiance enters the water. As the Sun sinks lower in the sky, the Fresnel reflectance increases rapidly and less of the direct solar beam enters the water. This results in the continuing decrease in transmittance until the minimum is reached. However, when the Sun is very near the horizon, the sky radiance is then almost entirely diffuse, so that radiance is coming from all directions—in particular from near-zenith directions for which the Fresnel reflectance is small.

A higher fraction of the total radiance thus begins to enter the water as Sun nears the horizon and the radiance becomes increasingly diffuse.

Most global-scale, long-term ecosystem simulations use daily averaged irradiances rather than instantaneous values. Daily averages were computed as follows. For a given latitude and day of year, the time of sunrise was computed using standard astronomical formulas. The first call to EcoLight-S was then made 15 min after sunrise. Subsequent calls were made at 30 min intervals, with the last call being set to local noon. The irradiances at the computed times (appending a value of 0 at sunrise) were then spline fit and numerically integrated to obtain the averages over 24 h, which we denote by $\langle E\rangle_{24}$ or $\langle \mathrm{PAR}\rangle_{24}$. Polar regions with 24 h of summer daylight had computations every 30 min from midnight to noon. Figure 3 shows example instantaneous $E_d(\mathrm{air})$ values for selected latitudes and days of the year. The curves are symmetric from local noon to sunset. The dots show the computed values; the lines are the spline fits used to compute daily averages.

For each EcoLight-S simulation, results were saved at each computed time for $E_d(\mathrm{air})$, $E_d(0)$, $E_{\mathrm{net}}(0)$, $\mathrm{PAR}_d(\mathrm{air})$, $\mathrm{PAR}_d(0)$, $\mathrm{PAR}_o(\mathrm{air})$, $\mathrm{PAR}_o(0)$, $E_u(\mathrm{air})$, and $E_u(0)$. This allows the computation of the daily averaged above-surface $\langle E_d(\mathrm{air})\rangle_{24}$ and $\langle \mathrm{PAR}_d(\mathrm{air})\rangle_{24}$ and their conversion into in-water $\langle E_{\mathrm{net}}(0)\rangle_{24}$ and $\langle \mathrm{PAR}_o(0)\rangle_{24}$, which are the quantities of greatest interest for ecosystem and biogeochemical modeling. Other quantities of possible interest such as the irradiance reflectance $\langle E_u\rangle_{24}/\langle E_d\rangle_{24}$ in air or water can also be computed if needed.

3. Surface Transmission Factors

The quantities relevant to ocean modeling are $E_{\mathrm{net}}(0)$ for heating calculations and $\mathrm{PAR}_o(0)$ for photosynthesis and photo-oxidation calculations. Most models are externally forced by either $E_d(\mathrm{air})$ (e.g., output from the RADTRAN atmospheric irradiance model) or $\mathrm{PAR}_d(\mathrm{air})$ (e.g., the NASA PAR product). There are thus four possible conversions that may be needed, depending on whether an ecosystem model is forced by above-surface light in energy or quantum units, and on whether the model includes both heating and photosynthesis calculations. We therefore present results for conversion of both $E_d(\mathrm{air})$ and $\mathrm{PAR}_d(\mathrm{air})$ to both $E_{\mathrm{net}}(0)$ and $\mathrm{PAR}_o(0)$. We first discuss results as a function of latitude for a few selected days of the year, and then we show annual patterns for the entire globe.

Figure 4(a) shows $\langle E_d(\mathrm{air})\rangle_{24}$ and $\langle E_{\mathrm{net}}(0)\rangle_{24}$ for a wind speed of $U = 0$, $\mathrm{Chl} = 0.5\ \mathrm{mg\,m^{-3}}$, and a clear sky. Figure 4(b) shows the surface transmission factor that converts above-surface $\langle E_d(\mathrm{air})\rangle_{24}$ to below-surface $\langle E_{\mathrm{net}}(0)\rangle_{24}$. Note in the top panel that there is a small asymmetry in the E values between the northern and southern hemispheres. This results from the Earth's elliptical orbit: Earth is closest to the Sun on 3 January and farthest on 4 July. This magnitude difference in incident sky irradiance scales the entire light field and thus does not affect the ratios seen in Fig. 4(b). The amount of above-surface E being transmitted below the surface ranges from about 95% for tropical and summer midlatitudes, to less than 80% near the latitude of 24 h darkness during the polar night (curves are not plotted beyond this latitude). The poleward increase from the minimum to the latitude of the polar night results from the combination of surface Fresnel reflectance and diffuseness of the incident sky radiance as was discussed in Fig. 2. Near the polar-night boundary, the Sun is very low in the sky during the entire day and the effect previously seen for instantaneous

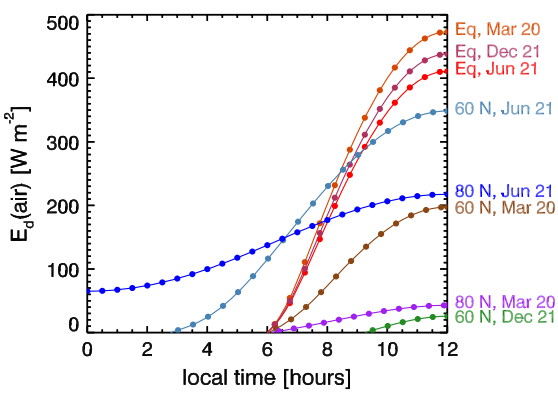

Fig. 3. (Color online) Above-surface E_d during the course of the day for selected latitudes and days of the year. Dots show the values computed by EcoLight-S; curves are the spline fits.

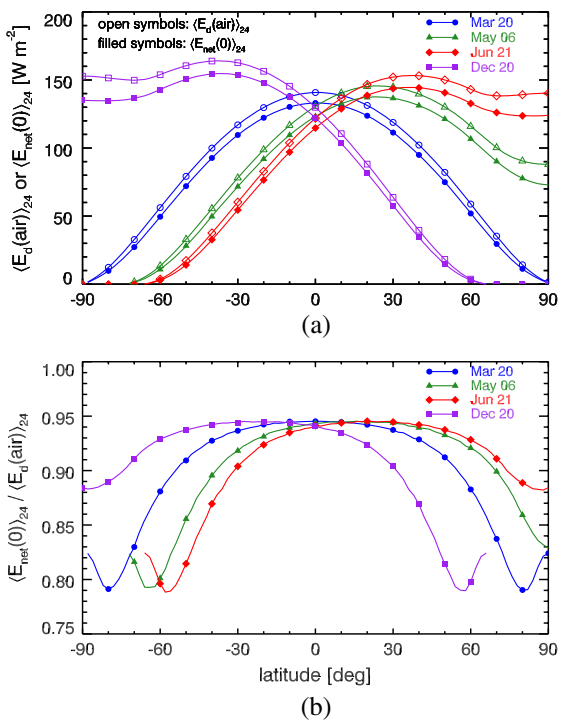

Fig. 4. (Color online) $\langle E_d(\mathrm{air})\rangle_{24}$ and $\langle E_{\mathrm{net}}(0)\rangle_{24}$ for a wind speed of $U = 0$, $\mathrm{Chl} = 0.5\ \mathrm{mg\,m^{-3}}$, and a clear sky. (a) Daily averaged E values. (b) Factor that converts above-surface $\langle E_d(\mathrm{air})\rangle_{24}$ to below-surface $\langle E_{\mathrm{net}}(0)\rangle_{24}$ values. Computations were at 2° latitude resolution; identifying symbols are plotted every 10° of latitude.

values with the Sun near the horizon carries over to the daily averages.

Figure 5 shows $\langle E_d(\mathrm{air})\rangle_{24}$, $\langle \mathrm{PAR}_o(0)\rangle_{24}$, and the corresponding conversion factors. The conversion factors now have units of mol photons day^{-1} W^{-1}, as needed to convert energy units of W m^{-2} to quantum units of mol photons m^{-2} day^{-1}. The factors also have a qualitatively different shape as a function of latitude than those of Fig. 4. This difference in shape results from the cos θ factor of Eq. (1), which reduces the contribution of near-horizontal radiance to E_d but which does not occur in E_o in Eq. (4). For the conversion factors of Fig. 4, both above- and below-surface quantities contain a cosine factor. For the factors of Fig. 5, only the above-surface quantity contains a cosine factor, whose effect becomes largest when the Sun remains low in the sky during the entire day. The exact shapes of the conversion factors in the lower panel of Fig. 5 result from the complex interplay of Fresnel reflectance, sky diffuseness, and the cosine factor.

Figure 6 shows PAR values above and below the surface and the factors that convert $\langle \mathrm{PAR}_d(\mathrm{air})\rangle_{24}$ to $\langle \mathrm{PAR}_o(0)\rangle_{24}$. The in-water PAR values are greater than the in-air values because $\langle \mathrm{PAR}_d(\mathrm{air})\rangle_{24}$ contains the previously discussed cos θ factor, which strongly reduces $\langle \mathrm{PAR}_d(\mathrm{air})\rangle_{24}$ magnitudes for large solar zenith angles. $\langle \mathrm{PAR}_o(0)\rangle_{24}$, on the other hand, is based on Eq. (4) and weights the radiance equally for all directions.

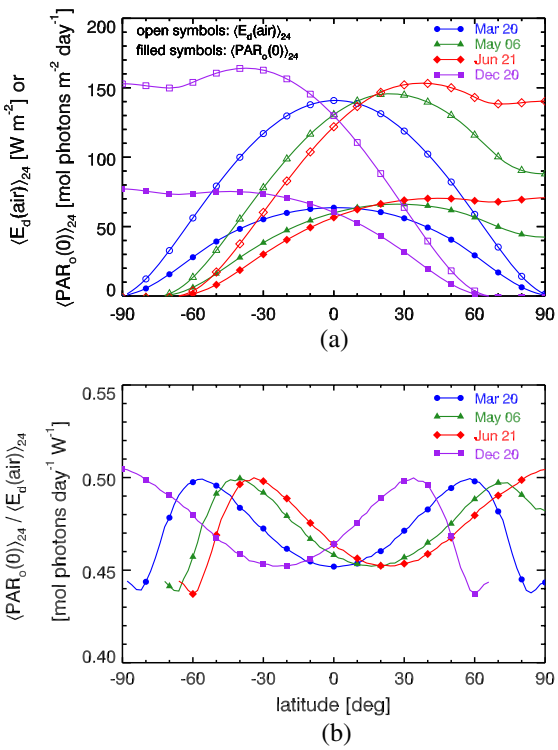

Fig. 5. (Color online) $\langle E_d(\mathrm{air})\rangle_{24}$, $\langle \mathrm{PAR}_o(0)\rangle_{24}$, and the corresponding conversion factors. The conversion factors now have units that convert the energy units of $\langle E_d(\mathrm{air})\rangle_{24}$ to the quantum units of $\langle \mathrm{PAR}_o(0)\rangle_{24}$. Environmental and other conditions are the same as for Fig. 4.

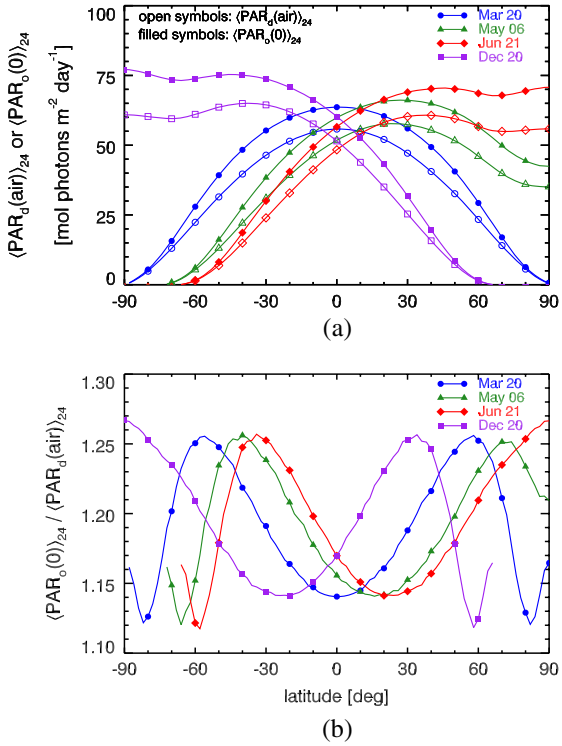

Fig. 6. (Color online) $\langle \mathrm{PAR}_d(\mathrm{air})\rangle_{24}$, $\langle \mathrm{PAR}_o(0)\rangle_{24}$, and the factors that convert $\langle \mathrm{PAR}_d(\mathrm{air})\rangle_{24}$ to $\langle \mathrm{PAR}_o(0)\rangle_{24}$. Other conditions are the same as for Fig. 4.

Finally, Fig. 7 shows the conversion from above-surface $\langle \mathrm{PAR}_d(\mathrm{air})\rangle_{24}$ to below-surface $\langle E_{\mathrm{net}}(0)\rangle_{24}$ values. The conversion factors are qualitatively similar in shape to those of Fig. 4 because both quantities contain the cosine factor. The units now convert quantum units to energy units.

The preceding four figures are all for zero wind speed, one chlorophyll concentration, and a clear sky. Figure 8 shows the effect of wind speed, chlorophyll concentration, and sky condition on the four types of surface transmission factors for one day, 21 June. Consider first Figure 8(a), which shows the factors for converting $\langle E_d(\mathrm{air})\rangle_{24}$ to $\langle E_{\mathrm{net}}(0)\rangle_{24}$. The curves with identifying symbols are for clear-sky conditions. As the wind increases from 0, i.e., a level sea surface, surface wave facets become tilted so that incident radiance (especially from near-horizon directions) can have a smaller incident angle relative to the surface normal. This allows, on average over many wave facets, more radiance to enter the water. The transmission factors thus increase with increasing wind speed. This effect is minimal for latitudes where the Sun is high in the sky for most of the day, but is significant at high latitudes where the Sun remains low in the sky. The curves for 0 and 15 m s^{-1} wind speeds show values for low, medium, and high chlorophyll values of 0.05, 0.5, and 5 mg m^{-3}. As anticipated from Fig. 1, the chlorophyll value has only a small effect on the conversion factors for $\langle E_{\mathrm{net}}(0)\rangle_{24}$ because that quantity is dominated by solar and sky irradiance transmitted through the

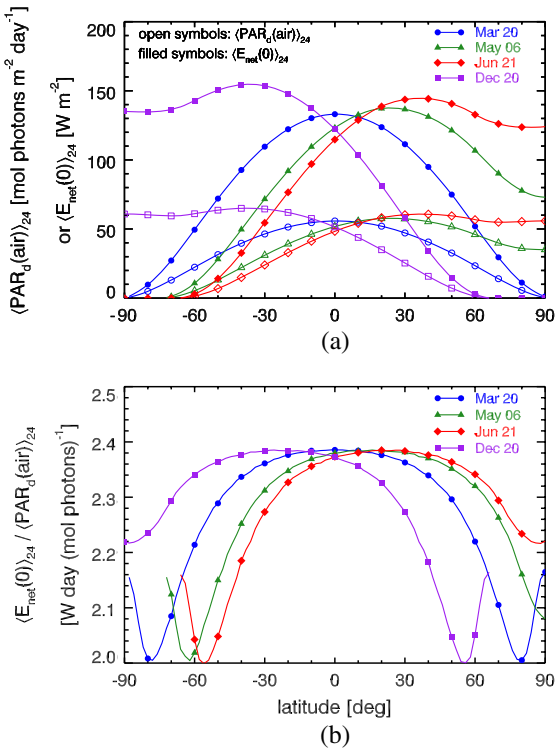

Fig. 7. (Color online) $\mathrm{PAR}_d(\mathrm{air})\rangle_{24}$, $\langle E_{\mathrm{net}}(0)\rangle_{24}$, and the factors that convert above-surface $\mathrm{PAR}_d(\mathrm{air})\rangle_{24}$ to below-surface $\langle E_{\mathrm{net}}(0)\rangle_{24}$ values. Other conditions are the same as for Fig. 4.

sea surface. The contribution of $\langle E_u(0)\rangle_{24}$, which is directly affected by chlorophyll (e.g., by backscatter from phytoplankton) is typically only a few percent of $\langle E_d(0)\rangle_{24}$.

The curves without identifying symbols show the results for a heavily overcast sky. The solid line is for $U = 0$, and the dashed–dotted line is for $15\ \mathrm{m\,s^{-1}}$. For an overcast sky, which has an approximately cardioidal radiance distribution, the maximum daily average irradiance values are less than $40\ \mathrm{W\,m^{-2}}$ (not shown). The transmission factors all collapse into values between 0.93 and 0.945, nearly independent of latitude and wind speed.

Figure 8(b) shows the factors for conversion of $\langle E_d(\mathrm{air})\rangle_{24}$ to $\langle \mathrm{PAR}_o(0)\rangle_{24}$. These factors now have units of mol photons $\mathrm{day^{-1}\,W^{-1}}$, as needed to convert the energy units of $\langle E_d(\mathrm{air})\rangle_{24}$ to the quantum units of $\langle \mathrm{PAR}_o(0)\rangle_{24}$. Figures 8(c) and 8(d) show the factors that convert $\langle \mathrm{PAR}_d(\mathrm{air})\rangle_{24}$ into $\langle \mathrm{PAR}_o(0)\rangle_{24}$ [Fig. 8(c)] and $\langle E_{\mathrm{net}}(0)\rangle_{24}$ [Fig. 8(d)]. All of these factors show a dependence on latitude and wind speed for clear skies, but much less dependence for overcast skies. In all cases, there is very little dependence on the chlorophyll value.

The preceding figures give a feeling for the dependence of surface transmission factors on latitude, day of year, sky condition, wind speed, and chlorophyll concentration, but for only a few selected days.

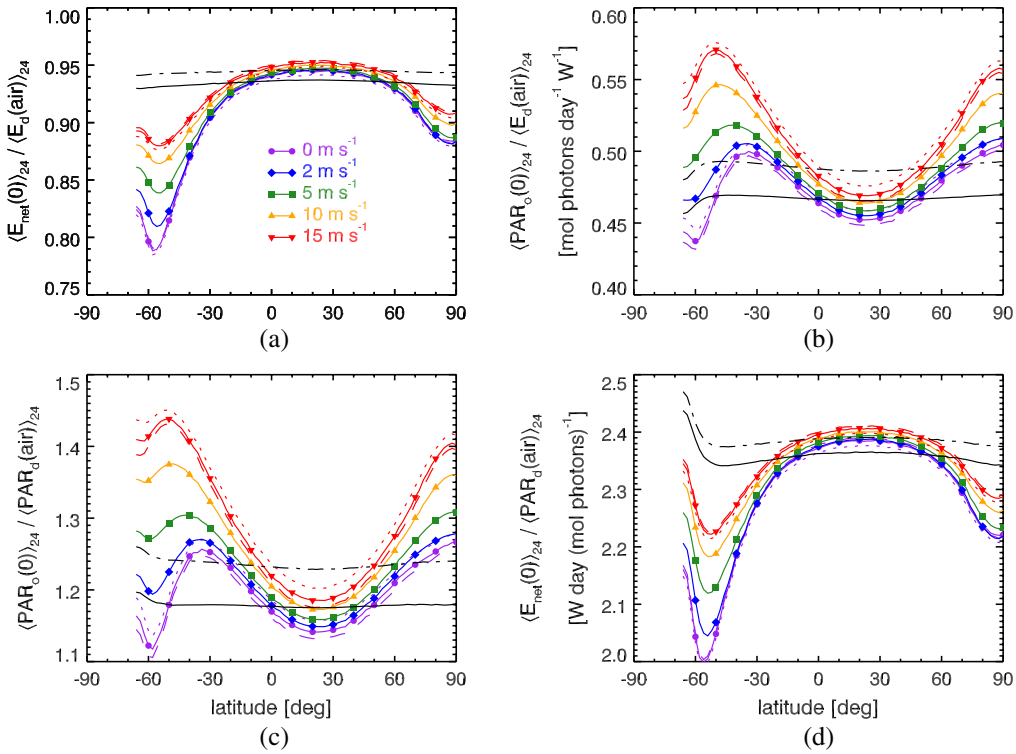

Fig. 8. (Color online) Surface transmission factors for the four types of conversions: (a) $\langle E_d(\mathrm{air})\rangle_{24}$ to $\langle E_{\mathrm{net}}(0)\rangle_{24}$, (b) $\langle E_d(\mathrm{air})\rangle_{24}$ to $\langle \mathrm{PAR}_o(0)\rangle_{24}$, (c) $\langle \mathrm{PAR}_d(\mathrm{air})\rangle_{24}$ to $\langle \mathrm{PAR}_o(0)\rangle_{24}$, and (d) $\langle \mathrm{PAR}_d(\mathrm{air})\rangle_{24}$ to $\langle E_{\mathrm{net}}(0)\rangle_{24}$. Curves with symbols and colors identifying the wind speed are for clear skies. The solid black curves without symbols are for an overcast sky and zero wind speed; the black dashed–dotted curves are for an overcast sky and $15\ \mathrm{m\,s^{-1}}$ wind speed. The clear-sky curves for 0 and $15\ \mathrm{m\,s^{-1}}$ wind speeds show values for low, medium, and high chlorophyll values of 0.05 (dotted lines), 0.5 (solid), and $5\ \mathrm{mg\,m^{-3}}$ (dashed). Other curves are for $\mathrm{Chl} = 0.5\ \mathrm{mg\,m^{-3}}$ All curves are for 21 June.

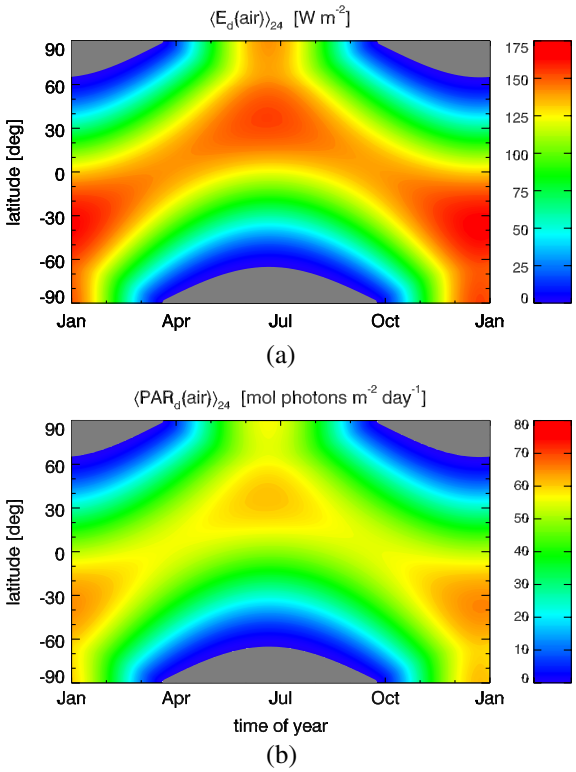

Fig. 9. The global annual patterns of $\langle E_d(\mathrm{air})\rangle_{24}$ and $\langle \mathrm{PAR}_d(\mathrm{air})\rangle_{24}$ as generated by EcoLight-S for a clear sky and zero wind speed. The gray areas are regions of 24 h darkness during the polar night.

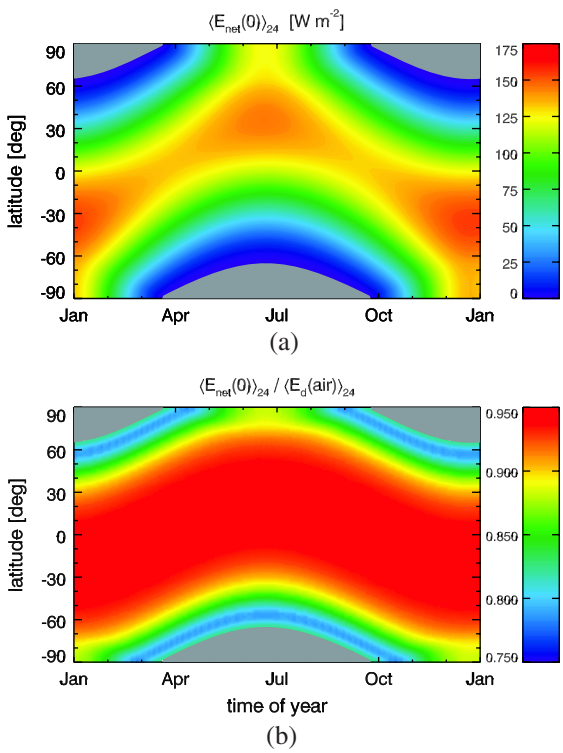

Fig. 10. (a) In-water $\langle E_{\mathrm{net}}(0)\rangle_{24}$ corresponding to Fig. 9(a). (b) Surface transmission factor that converts $\langle E_d(\mathrm{air})\rangle_{24}$ into $\langle E_{\mathrm{net}}(0)\rangle_{24}$.

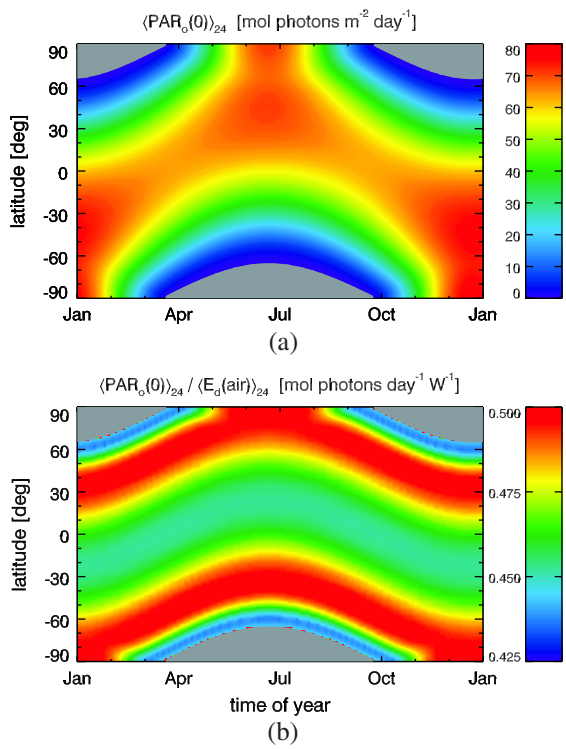

Fig. 11. (a) In-water $\langle \mathrm{PAR}_o(0)\rangle_{24}$ corresponding to Fig. 9(b). (b) Surface transmission factor that converts $\langle E_d(\mathrm{air})\rangle_{24}$ into $\langle \mathrm{PAR}_o(0)\rangle_{24}$.

Figure 9 shows the global annual pattern of above-surface $\langle E_d(\mathrm{air})\rangle_{24}$ and $\langle \mathrm{PAR}_d(\mathrm{air})\rangle_{24}$ as generated by EcoLight-S using its incorporated RADTRAN and semiempirical sky radiance models. The gray areas are regions of 24 h darkness during the polar night. The plots were generated from daily values at 2° latitude resolution. Figure 10(a) shows the corresponding $\langle E_{\mathrm{net}}(0)\rangle_{24}$, and Fig. 10(b) shows the surface transmission factor that converts the $\langle E_d(\mathrm{air})\rangle_{24}$ of Fig. 9 into $\langle E_{\mathrm{net}}(0)\rangle_{24}$. Figure 11 shows the corresponding in-water $\langle \mathrm{PAR}_o(0)\rangle_{24}$ and the factor that converts $\langle E_d(\mathrm{air})\rangle_{24}$ in units of $\mathrm{W\,m^{-2}}$ to $\langle \mathrm{PAR}_o(0)\rangle_{24}$ in units of mol photons $\mathrm{m^{-2}\,day^{-1}}$. These three figures are all for zero wind speed, $\mathrm{Chl} = 0.5\ \mathrm{mg\,m^{-3}}$, and a clear sky. The global annual patterns for conversions beginning with $\langle \mathrm{PAR}_d(\mathrm{air})\rangle_{24}$ are similar, differing only in magnitudes and units.

4. Summary

The daily averaged net irradiance $\langle E_{\mathrm{net}}(0)\rangle_{24}$ entering the ocean is roughly 5% to 20% less than the downwelling irradiance $\langle E_d(\mathrm{air})\rangle_{24}$ incident onto the sea surface. The exact amount entering the water depends primarily on latitude, day of the year, wind speed, and sky conditions. The largest percentage differences in incident and transmitted irradiance are near the edge of the polar-night boundary. These differences will give the same percentage difference in heating rates computed by Eq. (3). There is a similar spread of values for how much above-surface light is converted to below-surface $\langle \mathrm{PAR}_o(0)\rangle_{24}$.

Although the PAR values themselves are small near the edge of the polar-night boundary, they are nevertheless ecologically important. Aquatic photosynthesis occurs with PAR values as low as 0.4 mol photons m^{-2} day^{-1} [45], and less for some benthic biota [32], so even small PAR values influence the spring phytoplankton bloom and shallow-water benthic biota in polar waters after the end of the long polar night.

Surface-reflectance effects always result in less irradiance and PAR entering the ocean. Not accounting for surface effects lets too much light into the ocean and thus introduces a systematic bias toward more heating and more photosynthesis in model predictions. Moreover, the surface effects are lowest in equatorial regions and greatest near the latitude of the polar-night boundary. Proper accounting for surface effects may therefore enhance equator-to-pole gradients in model predictions. The arctic is changing especially rapidly, and the possibility of an ice-free summer Arctic Ocean within the next few decades makes it imperative that coupled hydrodynamic and biological models of that area use the best possible light inputs in studies of that important ecosystem. Indeed, a recent review of models for marine primary production [46] noted that "Specific concerns for future progress include improved formulation of the quantum yield and of the light field . . . ."

Present-day models used for climate studies and other global-scale simulations are limited in their realism by computational constraints. The need for improved accuracy in light values therefore must be addressed at almost no additional computational time. Most ocean models are forced by above-surface daily averaged irradiance or PAR obtained from climatology or satellite observations. In many previously published studies, little or no correction appears to have been made in transmitting above-surface values into the water, where irradiance was then propagated to depth by various simple optical models for $E_d(z)$ or PAR(z). These optical models generally take the in-water attenuation to be either a fixed diffuse attenuation function K or a simple parameterization in terms of the cholorphyll concentration. Although K functions depend on in-water absorption and scattering properties, near the sea surface they also depend the incident radiance distribution and sea-surface conditions. Gege [40] has shown how to improve parameterizations of $K_d(z)$ in terms of the contributions of direct (solar) and diffuse (sky) irradiance to the total in-water irradiance, so that the direct and diffuse parts decay with depth at different rates. His parameterization of $K_d(z)$ has been validated only for a few data sets and for a level sea surface (by comparison with HydroLight-computed values), but it could be extended to $K_o(z)$ and other wind speeds. Such a parameterization could be applied if the incident irradiance comes from models such as RADTRAN or OASIM, which provide separate calculations of direct and diffuse irradiance onto or below the sea surface. No GCM or global-scale ecosystem model has yet incorporated a radiative transfer module to accurately compute the in-water E_{net} or PAR distribution with depth as determined by the wind speed, sky condition, and biomass profile at the current time and location. Such improvements in model realism lie in the future.

We have therefore developed easily applied files of surface transmission functions that convert above-surface daily averaged $\langle E_d(\mathrm{air})\rangle_{24}$ and $\langle \mathrm{PAR}_d(\mathrm{air})\rangle_{24}$ values, regardless of how obtained, into below-surface (at depth zero, just below the mean sea surface) values of $\langle E_{\mathrm{net}}(0)\rangle_{24}$ and $\langle \mathrm{PAR}_o(0)\rangle_{24}$ as needed to initialize optical models for further propagation to depth. Models that resolve their external inputs during the course of the day can obtain transmission factors as a function of the instantaneous Sun zenith angle and other conditions from data like those of Fig. 2. These data files, as used to create the figures in this paper, can be downloaded from http://www.oceanopticsbook.info/view/radiative_transfer_theory/level_3/surface_transmission_factors. The files are available on a 2° latitude grid at daily resolution, for wind speeds of 0, 2, 5, 10, and 15 m s^{-1} and clear skies. It is probably sufficient to interpolate those values to the latitude grid used by a particular ecosystem model to create a file applicable to any particular ecosystem model. Those values can then be applied to the input above-surface irradiances via a simple multiplication to obtain the in-water values. Models driven by precomputed databases can apply the factors once to the above-surface database to obtain in-water values, which can then be read with no additional computation at all. Factors for overcast skies are almost independent of wind speed and latitude and can be set to average values read from Fig. 8 for the quantity of interest. Conversion factors for other quantities or particular computational grids can be easily created.

Author C.D.M. was supported by NASA contract NNH12CD06C. We are grateful to two anonymous reviewers for their helpful comments.

References

1. T. D. Dickey and P. G. Falkowski, "Solar energy and its biological-physical interactions in the sea," in *The Sea*, A. R. Robinson, J. J. McCarthy, and B. J. Rothschild, eds. (Wiley, 2002), pp. 401–440.
2. C. A. Paulson and J. J. Simpson, "Irradiance measurements in the upper ocean," J. Phys. Oceanogr. **7**, 952–956 (1977).
3. J. J. Simpson and T. D. Dickey, "The relationship between downward irradiance and upper ocean structure," J. Phys. Oceanogr. **11**, 309–323 (1981).
4. J. C. Ohlmann, D. A. Siegel, and C. D. Mobley, "Ocean radiant heating. Part I: Optical influences," J. Phys. Oceanogr. **30**, 1833–1848 (2000).
5. J. C. Ohlmann and D. A. Siegel, "Ocean radiant heating. Part II: Parameterizing solar radiation transmission through the upper ocean," J. Phys. Oceanogr. **30**, 1849–1865 (2000).
6. J. C. Ohlmann, "Ocean radiant heating in climate models," J. Clim. **16**, 1337–1351 (2003).
7. C. D. Mobley, B. Gentili, H. Gordon, Z. Jin, G. Kattawar, A. Morel, P. Reinersman, K. Stamnes, and R. Stavn, "Comparison of numerical models for the computation of underwater light fields," Appl. Opt. **32**, 7484–7504 (1993).

8. C. D. Mobley, *Light and Water: Radiative Transfer in Natural Waters* (Academic, 1994).
9. C. D. Mobley, Ocean Optics Web Book: HydroLight (2011), http://www.oceanopticsbook.info/view/radiative_transfer_theory/level_2/hydrolight.
10. E. K. Schneider and Z. Zhu, "Sensitivity of the simulated annual cycle of sea surface temperature in the equatorial Pacific to sunlight penetration," J. Clim. **11**, 1932–1950 (1998).
11. S. Nakamoto, S. P. Kumar, J. M. Oberhuber, K. Muneyama, and R. Frouin, "Chlorophyll modulation of sea surface temperature in the Arabian Sea in a mixed-layer isopycnal general circulation model," Geophys. Res. Lett. **27**, 747–750 (2000).
12. S. Nakamoto, S. P. Kumar, J. M. Oberhuber, J. Ishizaka, K. Muneyama, and R. Frouin, "Response of the equatorial Pacific to chlorophyll pigments in a mixed-layer isopycnal general circulation model," Geophys. Res. Lett. **28**, 2021–2024 (2001).
13. R. Murtugudde, J. Beauchamp, C. R. McClain, M. Lewis, and A. J. Busalacchi, "Effects of penetrative radiation on the upper tropical ocean circulation," J. Clim. **15**, 470–486 (2002).
14. P. A. Rochford, A. B. Kara, A. J. Wallcraft, and R. A. Arnone, "Importance of solar subsurface heating in ocean general circulation models," J. Geophys. Res. **106**, 30923–30938 (2001).
15. A. B. Kara, A. J. Wallcraft, and H. E. Hurlburt, "A new solar radiation penetration scheme for use in ocean mixed layer studies: An application to the Black Sea using a fine-resolution hybrid coordinate ocean model (HYCOM)," J. Phys. Oceanogr. **35**, 13–32 (2005).
16. C. Sweeney, A. Gnanadesikan, S. M. Griffies, M. J. Harrison, A. J. Rosati, and B. L. Samuels, "Impacts of shortwave penetration depth on large-scale ocean circulations and heat transport," J. Phys. Oceanogr. **35**, 1103–1119 (2005).
17. A. Oschlies, "Feedbacks of biotically induced radiative heating on upper-ocean heat budget, circulation, and biological production in a coupled ecosystem-circulation model," J. Geophys. Res. **109**, C12031 (2004).
18. M. Manizza, C. L. Quéré, A. J. Watson, and E. T. Buitenhuis, "Bio-optical feedbacks among phytoplankton, upper ocean physics and sea-ice in a global model," Geophys. Res. Lett. **32**, L05603 (2005).
19. G. Danabasoglu, W. G. Large, J. J. Tribbia, P. R. Gent, and B. P. Briegleb, "Diurnal coupling in the tropical oceans of CCSM3," J. Clim. **19**, 2347–2365 (2006).
20. K. M. Shell, F. Frouin, S. Nakamoto, and R. C. J. Somerville, "Atmospheric response to solar radiation absorbed by phytoplankton," J. Geophys. Res. **108**, 4445–4452 (2003).
21. P. Wetzel, E. Maier-Reimer, M. Botzet, and J. Jungclaus, "Effects of ocean biology on the penetrative radiation in a coupled climate model," J. Clim. **19**, 3973–3987 (2006).
22. M. Jochum, S. Yeager, K. Lindsay, K. Moore, and R. Murtagudde, "Quantification of the feedback between phytoplankton and ENSO in the Community Climate System Model," J. Clim. **23**, 2916–2925 (2010).
23. W. W. Gregg and N. W. Casey, "Skill assessment of a spectral ocean-atmosphere radiative model," J. Marine Syst. **76**, 49–63 (2009).
24. W. W. Gregg and K. L. Carder, "A simple spectral solar irradiance model for cloudless maritime atmospheres," Limnol. Oceanogr. **35**, 1657–1675 (1990).
25. W. W. Gregg, "Tracking the SeaWiFS record with a coupled physical/biogeochemical/radiative model of the global oceans," Deep-Sea Res. II **49**, 81–105 (2001).
26. "GMAO ocean biology and biogeochemical modeling" (2012), https://gmao.gsfc.nasa.gov/research/oceanbiology/.
27. C. D. Mobley, "Fast light calculations for ocean ecosystem and inverse models," Opt. Express **19**, 18927–18944 (2011).
28. M. Fujii, E. Boss, and F. Chai, "The value of adding optics to ecosystem models: A case study," Biogeosciences **4**, 817–835 (2007).
29. C. D. Mobley, L. K. Sundman, W. P. Bissett, and B. Cahill, "Fast and accurate irradiance calculations for ecosystem models," Biogeosci. Discuss. **6**, 10625–10662 (2009).
30. C. D. Mobley and F. Chai, "Improved ocean ecosystem predictions via improved optics," to be presented at Ocean Optics XXI, Glasgow, Scotland, 8–12 October 2012.
31. M. J. Behrenfeld, T. K. Westbury, E. S. Boss, R. T. O'Malley, D. A. Siegel, J. D. Wiggert, B. A. Franz, C. R. McClain, G. C. Feldman, S. C. Doney, J. K. Moore, G. Dall'Olmo, A. J. Milligan, I. Lima, and N. Mahowald, "Satellite-detected fluorescense reveals global physiology of ocean phytoplankton," Biogeosciences **6**, 779–794 (2009).
32. J.-P. Gattuso, B. Gentili, C. M. Duarte, J. A. Kelypas, J. J. Middelburg, and D. Antoine, "Light availability in the coastal ocean: Impact on the distribution of benthic photosynthetic organisms and their contribution to primary production," Biogeosciences **3**, 489–513 (2006).
33. K. Mopper and D. J. Kieber, *Marine Photochemistry and Its Impact on Carbon Cycling* (Cambridge University, 2000).
34. P. Coble, "Marine optical biogeochemistry: The chemistry of ocean color," Chem. Rev. **107**, 402–418 (2007).
35. R. Frouin, B. A. Franz, and J. Werdell, "The SeaWiFS PAR product," in NASA Technical Memo 2003–206892, Vol. 22: Algorithm Updates for the Fourth SeaWiFS Data Reprocessing, S. B. Hooker and E. R. Firestone, eds. (NASA Goddard Space Flight Center, 2003), pp. 50–54.
36. J. Aiken and G. Moore, "ATBD photosynthetically available radiation (PAR)," Technical report (Plymouth Marine Lab, 1997).
37. C. D. Mobley, "EcoLight-S 1.0 users' guide and technical documentation," Technical report (Sequoia Scientific, Inc., 2011), http://www.sequoiasci.com/products/els-radiative.cmsx.
38. C. Cox and W. Munk, "Measurement of the roughness of the sea surface from photographs of the sun's glitter," J. Opt. Soc. Am. **44**, 838–850 (1954).
39. C. Cox and W. Munk, "Statistics of the sea surface derived from sun glitter," J. Mar. Res. **13**, 198–227 (1954).
40. P. Gege, "Analytic model for the direct and diffuse components of downwelling spectral irradiance in water," Appl. Opt. **51**, 1407–1419 (2012).
41. F. Kasten and G. Czeplak, "Solar and terrestrial radiation dependent on the amount and type of cloud," Sol. Energy **24**, 177–189 (1980).
42. A. W. Harrison and C. A. Coombes, "Angular distribution of clear sky short wavelength radiance," Sol. Energy **40**, 57–63 (1988).
43. A. W. Harrison and C. A. Coombes, "An opaque cloud cover model of sky short wavelength radiance," Sol. Energy **41**, 387–392 (1988).
44. C. D. Mobley, "Ocean optics web book: A new IOP model for Case 1 water," 2010, http://www.oceanopticsbook.info/view/optical_constituents_of_the_ocean/__level_2/a_new_iop_model_for_case_1_water.
45. R. M. Letelier, D. M. Karl, M. R. Abbot, and R. R. Bidigare, "Light driven seasonal patterns of chlorophyll and nitrate in the lower euphotic zone of the North Pacific Subtropical Gyer," Limnol. Oceanogr. **49**, 508–519 (2004).
46. M.-E. Carr, M. A. M. Friedrichs, M. Schmeltz, M. N. Aita, D. Antoine, K. R. Arrigo, I. Asanuma, O. Aumont, R. Barber, M. Behrenfeld, R. Bidigare, E. T. Buitenhuis, J. Campbell, A. Ciotti, H. Dierssen, M. Dowell, J. Dunne, W. Esaias, B. Gentili, W. Gregg, S. Groom, N. Hoepffner, J. Ishizaka, T. Kameda, C. L. Quéré, S. Lorenz, J. Marra, F. Mélin, K. Moore, A. Morel, T. E. Reddy, J. Ryan, M. Scardi, T. Smyth, K. Turpie, G. Tilstone, K. Waters, and Y. Yamanaka, "A comparison of global estimates of marine primary production from ocean color," Deep-Sea Res. II **53**, 741–770 (2006).